RSC Advances

PAPER

View Article Online
View Journal | View Issue

Cite this: *RSC Adv.*, 2019, **9**, 30195

Large exchange bias and enhanced coercivity in strongly-coupled Ni/NiO binary nanoparticles

Xuemin He,[ab] Yingru Xu,[c] Xiujuan Yao,[b] Chuangwei Zhang,[a] Yong Pu,*[a] Xingfu Wang,[a] Weiwei Mao,[a] Youwei Du[b] and Wei Zhong *[b]

Received 30th April 2019
Accepted 18th September 2019

DOI: 10.1039/c9ra03242h

rsc.li/rsc-advances

In this study, Ni/NiO binary nanoparticles are synthesized utilizing a reflux method combined with a calcination process. The average size of the nanoparticles is 5–20 nm and the Ni content is 3.55%. Both the microstructures of the Ni/NiO interface and the states of different phases have significant impacts on the magnetic properties. By tuning the temperature and the cooling field during the loop measurement, the change rule of several critical parameters such as coercivity H_C and exchange bias H_E was complicated in nature. Both large H_E (482 Oe) and enhanced H_C (1335 Oe) were observed at 5 K, mainly due to the strong coupling interaction between Ni and NiO components. For current studies of the Ni/NiO binary nanoparticles, the complex magnetic behaviors are related to (i) the ferromagnetic contribution of Ni nanoparticles, (ii) the intrinsic antiferromagnetism of the volume phase of NiO, and (iii) the spin-glass-like characteristic corresponding to the frozen disordered state at the surface of partial NiO particles. The comprehensive effect of these three magnetic structures promotes the generation of a strongly-coupled Ni/NiO binary system, and improves the magnetic performance.

1. Introduction

Over the past few decades, functional nanocomposites have attracted increasing attention both in first principles and practical applications,[1–4] because of their great potential in new technologies. Magnetic nanoparticles with a core–shell (or compound, or binary) structure have been studied extensively.[5–8] In particular particle systems consisting of 3d transition metals and their oxides have shown the exchange bias (EB) effect and related phenomena with interesting applications, which can improve the performance of permanent magnetic materials, *i.e.* an enhancement of the coercivity – typically a shift of hysteresis loop,[9,10] and combating the superparamagnetic limit in magnetic recording media.[11,12] The Co/CoO core–shell structure is one of the most thoroughly studied systems whose EB behavior was observed in the core–shell structure at the ferromagnetic/antiferromagnetic (FM/AFM) interface for the first time.[13] Here we report a comprehensive study of the Ni/NiO particle system with distinguishable characteristics from Co/CoO and other relevant structures: compared with the Fe and Co nanoparticles that ignite spontaneously in air, Ni nanoparticles have better stability and resistance to oxidization[14] and its oxide, NiO, has a higher Néel temperature T_N (523 K) than typical 3d transition oxides like CoO (293 K) and FeO (198 K),[15] which enables the Ni/NiO system to generate a robust EB effect even at room temperature. In addition, the weaker anisotropy of NiO compared to CoO may lead to the observed anomalous magnetic properties.[16] Therefore, the investigation on the exchange bias of Ni/NiO particle system is of great interest not only for the loop shift itself, but also for other EB-related phenomena.

The magnetic properties of Ni/NiO nanoparticles are mainly determined by the microstructural features of both components, as well as the interface (*e.g.* contact mode, area, roughness, *etc.*). These factors are critical especially in nanosized crystals and are strongly affected by the synthetic route. Remarkable progress has been made in recent years regarding the synthesis of the Ni/NiO binary manoparticles.,[10,12,17–20] Highly crystalline and monodisperse Ni/NiO nanoparticles have been prepared by the physical techniques including laser-induced reductive sintering,[3] sequential layer deposition,[10] CVD method,[21] nanosecond laser irradiation,[22] cluster-beam deposition,[23] and pulsed laser deposition.[24] However, universal agreement of the origin of the EB effect and other related anomalous magnetic properties is still under debate. In addition the chemical synthesis methods of Ni/NiO nanoparticles are under development for instance, sol–gel route,[20,25,26] solution-combustion synthesis,[27,28] chemical reduction method,[12,18,29] solvothermal/thermal treatment process,[30] thermal decomposition,[31,32] electrodeposition technique,[4,17] *etc.* These chemical methods could be used for effective control of microstructures but the correlation between

[a]*New Energy Technology Engineering Laboratory of Jiangsu Province, Research Center of Information Physics, School of Science, Nanjing University of Posts and Telecommunications, Nanjing 210023, P. R. China. E-mail: puyong@njupt.edu.cn*

[b]*National Laboratory of Solid State Microstructures, Nanjing University, Nanjing 210093, P. R. China. E-mail: wzhong@nju.edu.cn*

[c]*Department of Physics, Duke University, Durham, NC 27713, USA*

microstructural parameters and magnetic properties has not yet been studied systematically.

It is well established that EB effect is the horizontal shift of hysteresis loop because of the exchange interaction at the FM/AFM interface, giving rise to a unidirectional anisotropy for the FM component.[9,33] As described here, the magnitude of this shift is defined as H_E. Accompanying the loop shift are other related behaviors. Probably the most common one in the nanoparticle systems is the enhancement of coercivity H_C, below the T_N of AFM material after a field cooling process. Without exception, for the Ni/NiO nanoparticles, if the sample is cooled in zero field from a demagnetized FM state, no EB effect is observed.[34,35] However, the EB behavior can be observed by field-cooling (FC) in a field H_{cool} aligning the magnetic moments of nanoparticles, which indicates the dependence of the EB effect, as well as related magnetic behaviors on the test temperature T and the cooling field H_{cool}. Yet unfortunately, few works were reported on the relationship between them, there are controversies even in reports that mention it.[34,36–40] Predictably the application of Ni/NiO nanoparticles could be extended once the above relationship is ascertained.

Herein, based on the Ni/NiO binary nanoparticles prepared by a reflux/calcination process, we systematically studied their microstructures and magnetic properties according to the comprehensive characterizations. The relationship between microstructural characteristics (for example, particle size, Ni content, interface quality, and contact form) and magnetic parameters (saturation magnetization M_s, remanent magnetization M_r, coercivity H_C, and so on) were analyzed in detail. We focus on the influences of test temperature T and cooling field H_{cool} on the exchange bias effect as well as the related behaviors in terms of synergistic effect of three factors. As a consequence, the Ni/NiO binary nanoparticles exhibit high H_E and enhanced H_C.

2. Experimental section

2.1 Sample preparation

All the analytical chemicals were purchased from the commercial market (Sinopharm Chemical Reagent Ltd, China) and used without further purification. In a typical synthesis process, 5 mmol nickel(II) acetate tetrahydrate ($Ni(CH_3COO)_2 \cdot 4H_2O$, AR, ≥98.0%) was dissolved in 2.5 mol ethylene glycol ($HOCH_2$-CH_2OH, AR, ≥99.5%) by vigorous stirring at room temperature for 30 min. Following this dissolution, the green solution was transferred into a 500 mL three-necked flask. Where the bottom of flask was merged into heat conduction oil (dimethyl silicone oil, $[OSi(CH_3)_2]_n$) for a heating-up, the center neck was connected to a water condenser for cycling the evaporated ethylene glycol back to the flask, and the remaining two necks were used for the insertion of thermocouple and thermometer, respectively. Accompany with the constant magnetic stirring, the solution was heated up to 170 °C (oil bath temperature) at a heating rate of 5 °C min^{-1} and kept at this temperature for 6 h. Then, the reaction mixture was cooled down to room temperature, and the obtained green precipitate was separated upon the addition of absolute ethanol, centrifuged, and washed using deionized water and absolute ethanol. The formed green product was dried under vacuum at 60 °C overnight, and the resultant substance was subject to grinding. At the end, the intermediate green powder was heated up to 300 °C at a heating rate of 6 °C min^{-1} and calcined in air at this temperature for 4 h to obtain Ni/NiO nanoparticle sample.

2.2 Microstructural characterization

X-ray diffraction (XRD) pattern was determined using a Philips X'pert diffractometer equipped with a rotating anode and Cu Kα radiation (40 kV, 40 mA, $\lambda = 1.54056$ Å). Based on the information of the standard cards (Ni, $Fm\bar{3}m(225)$, $a = 3.523$ Å, JCPDS no. 04-0850; NiO, $Fm\bar{3}m(225)$, $a = 4.177$ Å, JCPDS no. 47-1049), the data from the XRD analysis were subsequently refined using the classical Rietveld method, and thus microstructural parameters such as the average crystallite size, the lattice constant, and the phase content can be obtained. X-ray photoelectron spectroscopy (XPS) was recorded in a Kratos Axis Ultra DLD spectrophotometer using the Al Kα radiation. The particle shape was imaged with a FEI Sirion200 scanning electron microscope (SEM) operating at an accelerating voltage of 5 kV. For transmission electron microscope (TEM) investigation, a drop of the tested powder sample in ethanol was deposited on each carbon-coated copper grid and then dried in air. Based on the JEOL JEM-2100 instrument, high-resolution TEM (HRTEM) in conjunction with selected-area electron diffraction (SAED) analyses were used to determine the local microstructure and crystallographic phase.

2.3 Magnetic measurement

Based on the MPMS-XL superconducting quantum interference device (SQUID) and the Quantum Design physical properties measurement system (PPMS), the magnetic properties were recorded for powder sample in gelatin capsule, and the magnetization M was measured against the magnetic field H and the temperature T. More specifically, it mainly including the following five aspects: (i) SQUID measured room-temperature (300 K) hysteresis (M–H) loop in a magnetic field up to ±10 000 Oe; (ii) low-temperature (*e.g.* $T = 5$, 50, 100, 150, 200, 250 K); M–H loops under zero-field-cooling (ZFC) and field-cooling (FC, from 350 K in a field of $H_{cool} = 30$ kOe); (iii) 5 K loops under FC process by using different cooling fields (*e.g.* $H_{cool} = 10$, 20, 30, 40, 50, 60 kOe); (iv) ZFC and 500 Oe FC magnetization (M–T) curves in the range 2–350 K; and (v) ac susceptibility (χ'–T) curves at different frequencies (*e.g.* $f = 100$, 1000, 5000, and 10 000 Hz) in the 2–350 K temperature range, applying an ac magnetic field of 10 Oe.

3. Results and discussion

3.1 Microstructural analysis

The XRD pattern for the prepared sample is shown in Fig. 1(a). Two sets of diffraction peaks suggest that the sample is composed of Ni and NiO phases. Among them, the five obvious and broad peaks at 2θ, 37.249, 43.276, 62.879, 75.416 and 79.409 are corresponding to the (111), (200), (220), (311) and (222)

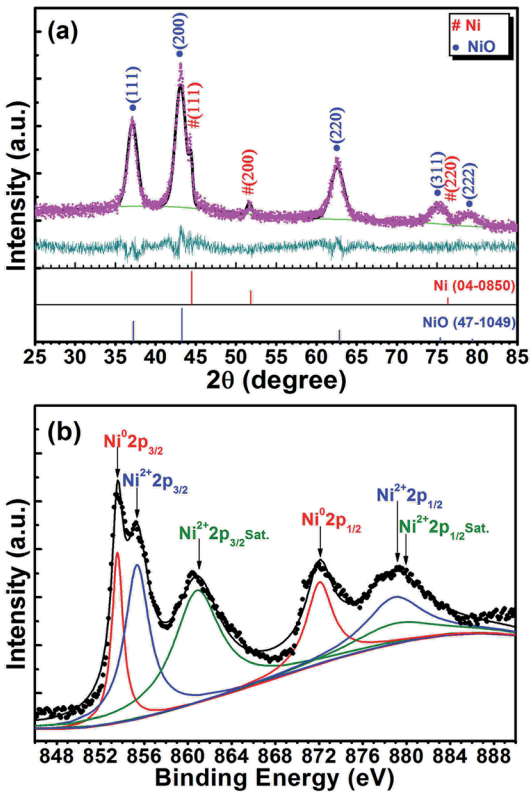

Fig. 1 (a) XRD pattern showing the results of the Rietveld profile refinement, and (b) XPS spectrum displaying the deconvoluted results of Ni 2p region for the Ni/NiO binary nanoparticles.

crystalline planes of NiO (JCPDS card no. 47-1049), and the other three weak diffraction peaks at 44.505 (111), 51.844 (200) and 76.366 (220) matches with metallic nickel phase (JCPDS card no. 04-0850). As for the present, both Ni and NiO phases have face-centered cubic (*fcc*) crystal structure with $Fm\bar{3}m(225)$ space group. Based on this, the microstructural parameters such as the average crystallite size (d), lattice constant (a), lattice volume (V), density (ρ) and relative content (wt%) of the two (Ni and NiO) phases can be determined according to the Rietveld refinement. The refined XRD pattern is also shown in Fig. 1(a), and the quantitative results of the refinement are listed in Table 1. For comparison, at the same time, the relevant data of bulk Ni and NiO are also given in Table 1.

Based on the peak shape parameter obtained by Rietveld refinement, the crystallite size can be calculated from the Debye–Scherrer formula using the full width at half maximum (FWHM) in the peaks. As shown in Table 1, the average sizes of Ni and NiO crystallites (d values) are 18.2 nm and 7.6 nm, respectively. On this one, we find these sizes in excellent agreement with the following HRTEM observations. Plenty of literatures prove that the average grain sizes of Ni and NiO phases are very small (generally 5–50 nm) for the Ni/NiO nanocomposites synthesized by different methods.[31,43–45] Accordingly, it should be obvious that such a small crystallite size contributes to the enhancement of size effect and surface effect for the Ni/NiO nanoparticles, and further affects the performance of composite materials, like optical, catalytic, and magnetic properties.

A little larger a-value of Ni, *viz.*, 3.540 Å, lies in comparison to a value of 3.523 Å in bulk Ni (JCPDS card no. 04-0850). This corresponds to $V = 44.36$ Å^3 ($\rho = 8.790$ g cm^{-3}), with $Z = 4$ units, in comparison to $V = 43.76$ Å^3 ($\rho = 8.911$ g cm^{-3}) in bulk Ni. Similarly, the NiO phase shows a larger a-value, *viz.*, 4.192 Å, in comparison to 4.177 Å in bulk NiO (JCPDS card no. 47-1049). Meanwhile, this corresponds to $V = 73.67$ Å^3 ($\rho = 6.735$ g cm^{-3}), with $Z = 4$ units, in comparison to $V = 72.88$ Å^3 ($\rho = 6.808$ g cm^{-3}) in bulk NiO. Obviously, both Ni and NiO phases have some degree of lattice expansion. It is well known that the lattice expansion in nanoparticles has been attributed to a number of possible phenomena including size confinement effects, grain surface relaxation, formation of point defects, and uncompensated Coulombic interactions.[46–48] However, in the present Ni/NiO sample, the observed <1.5% increase in the V-values of Ni and NiO (Ni: (44.36–43.76)/43.76 = 1.37%; NiO: (73.67–72.88)/72.88 = 1.08%) over that of their bulk counterparts is predominantly due to the interfacial interaction (interface between Ni and NiO). This kind of interaction causes two types of strains in the lattice.[49,50] One is the macrostrain, which increases the interplanar spacings (d_{hkl}), and the other is the microstrain, which induces a peak broadening. These judgments have been demonstrated in the XRD pattern, or will be confirmed by the subsequent TEM analysis.

Further analysis of the XRD data was processed with the Rietveld method using the GSAS program, to estimate the relative content of Ni and NiO phases in the Ni/NiO binary nanoparticles. As given in Table 1, the present Ni/NiO sample has a relative content (wt%) of Ni and NiO of 3.66% and 96.34%, respectively. This result is very close to that of magnetic analysis. In view of the fact that the sample is binary Ni/NiO nanoparticles with very low Ni content, it will show excellent magnetic properties. This phenomenology has been confirmed by many works related to the Ni–NiO system.[31,51,52]

XPS is an interesting tool that can provide insight into the chemical composition and electronic nature of the materials. In order to assess the chemical charge states of Ni element in the

Table 1 Results of the Rietveld analysis of the XRD pattern for the Ni/NiO binary nanoparticles

Category	d (nm)	a (Å)	V (Å^3)	ρ (g cm^{-3})	wt (%)	Ref.
Ni phase	18.2	3.540	44.36	8.790	3.66	Present work
NiO phase	7.6	4.192	73.67	6.735	96.34	Present work
Bulk Ni	—	3.523	43.76	8.911	—	JCPDS (card 04-0850)[41]
Bulk NiO	—	4.177	72.88	6.808	—	JCPDS (card 47-1049)[42]

synthesized nanoparticles, XPS characterization was employed. Fig. 1(b) shows the XPS spectrum of Ni 2p energy level of the sample. To get more information, the XPS data has been analyzed by the deconvolution method and the results are also shown in Fig. 1(b). Obviously, the obtained Ni 2p spectrum for the present Ni/NiO sample can be divided into two spin–orbit coupling regions, referred to as Ni $2p_{3/2}$ ($\approx$848–868 eV) and Ni $2p_{1/2}$ ($\approx$868–888 eV).[53] Focusing our attention to the Ni $2p_{3/2}$ core-level spectra, four Ni species have been reported in the XPS spectra of various nickel-containing samples: (i) metallic nickel (Ni^0) that appears at binding energy (BE) values of 852–854 eV, (ii) NiO at BE values in the range of 854–856 eV, (iii) $Ni(OH)_2$ at BEs of 856–858 eV, and (iv) satellite peaks correspond to Ni^{2+} at 860–862 eV.[31,43,44,51,54,55] Concretely speaking, in the present XPS spectrum, the peak at 853.6 eV is attributed to metallic Ni^0, the peak at 855.4 eV corresponds to Ni^{2+} (NiO), and the peak at 861.1 eV could be assigned to the shake-up satellite peak of Ni^{2+}. The presence of the highly intense satellite are consistent with the appearance of Ni^{2+} in the high-spin state, and it implies that in the present Ni/NiO sample there exist relatively high content of NiO component. This result shows good agreement with the above XRD analysis. Moreover, the characteristic peak of $Ni(OH)_2$ has not been observed in the total XPS spectrum. This confirms that we have successfully synthesized the Ni/NiO binary nanoparticles.

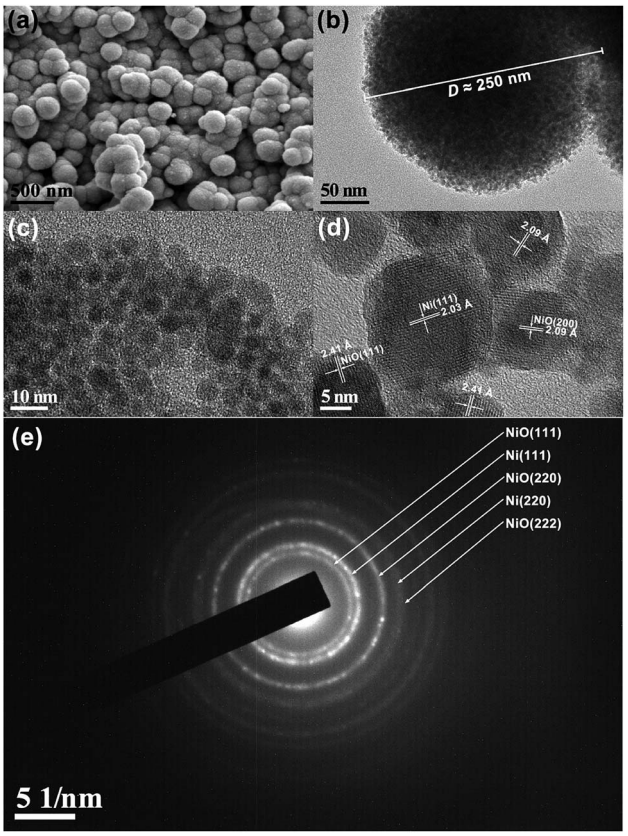

Fig. 2 (a) SEM image, (b) TEM image, (c) high-magnification TEM image, (d) high-resolution lattice image, and (e) SAED pattern of Ni/NiO binary nanoparticles.

The typical SEM image in Fig. 2(a) reveals that the sample is spherical particles in submicron size. Those particles have rough surface, which suggests that the microspheres are made up of smaller particles. Fig. 2(b) shows the TEM image of single microsphere with diameter of about 250 nm. Indeed, one can see random gathering of nanoparticles, in agreement with the SEM observation. The high-magnification TEM image in Fig. 2(c) depicts the size of those nanoparticles. This image clearly indicates that the nanoparticles with size ranging from 5 to 20 nm, accompanied by a good cross between those particles. As shown in Fig. 2(d), the high-resolution lattice image reveals the [111] orientation of Ni phase, as well as the [111] and [200] orientations of NiO phase. Specifically, there is intersection of the lattice fringes of Ni and NiO. Fig. 2(e) shows a typical SAED pattern corresponding to the Ni/NiO sample, consisting of some distinct concentric rings with discontinuous spots over the rings. As marked therein, these diffraction rings appear due to reflections from (111), (220) and (222) planes of the NiO phase, and the (111) and (220) planes of the Ni phase for the composite structure. Analogous SAED patterns are also observed in other Ni/NiO systems.[44,45,52] These results further confirm the coexistence of Ni and NiO phases in the obtained sample, as well as the formation of Ni/NiO interface. From the above TEM investigation, both structure and shape are consistent with the results of XRD, XPS and SEM analyses. Considering the fact that the sample is of good Ni/NiO interface, it will show excellent magnetic properties.

3.2 General analysis of magnetic properties

The room-temperature (300 K) hysteresis loop of Ni/NiO binary nanoparticles was measured by SQUID, the results are shown in Fig. 3(a). The loop contains the contributions of two magnetic phases, where the total magnetization is defined as $M(H) = M_{FM}(H) + \chi_{AF}H$.[56] Here M_{FM} is the magnetization due to ferromagnetic Ni and χ_{AF} is the susceptibility of antiferromagnetic NiO. χ_{AF} is determined by linear fitting the part of the loop with $H \geq 5000$ Oe.

As shown in the blue solid line in Fig. 3(a), M_{FM} saturates below 4000 Oe, which is similar to the saturation behavior of standard Ni sample. Based on this, the obtained saturation magnetization M_s is about 1.88 emu g^{-1}. Furthermore, the enlarged loop in the inset gives the values of remanent magnetization M_r and coercivity H_C; in this case, they are 0.54 emu g^{-1} and 323 Oe, respectively. The value of room-temperature coercivity has been found to be larger than the corresponding value of bulk Ni, $H_C = 100$ Oe.[15] Such coercivity enhancement is most likely originated from the nanostructure nature of the sample. Actually, only unoxidized atoms in the Ni contribute to the measured M_s, that is the relationship:[35]

$$\frac{N_{Ni}}{N_{Ni} + N_{NiO}} = \frac{M_s}{M_{sb}} \quad (1)$$

where N_{Ni} is the average number of Ni atoms in an unoxidized Ni particle, N_{NiO} is the average number of Ni atoms in the NiO particle, and M_{sb} is the saturation magnetization of bulk nickel. The above ratio can be viewed as the weight fraction of Ni in the

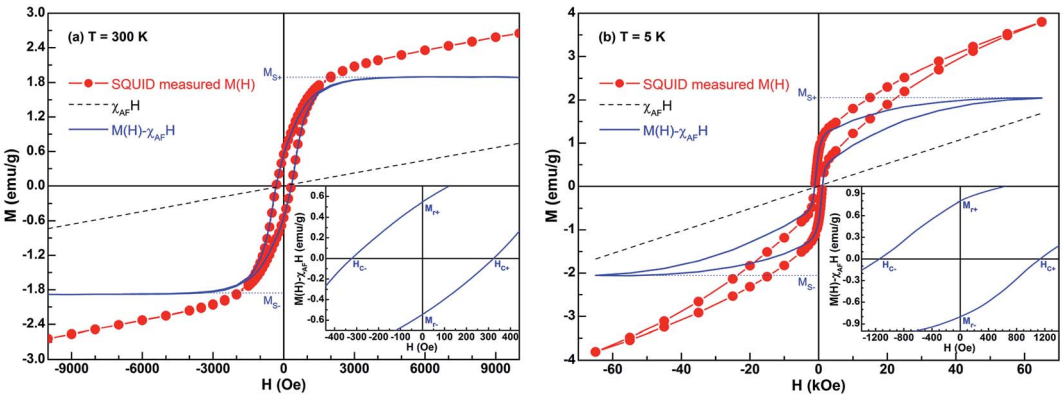

Fig. 3 (a) 300 K and (b) 5 K hysteresis loops of the Ni/NiO binary nanoparticles before and after subtracting the antiferromagnetic contribution, $\chi_{AF}H$. Insets show the enlarged loops displaying the corresponding coercivity and remanent magnetization.

Ni/NiO binary nanoparticle sample. Given that the M_{sb} at room temperature is 54.4 emu g^{-1},[57] the calculated Ni proportion is about 3.46%.

To decrease the effect of thermal disturbance on magnetic properties, the hysteresis loop at 5 K was also measured using a SQUID magnetometer with 70 kOe maximum field, the results are shown in Fig. 3(b). Obviously, the form of 5 K loop is similar to what happens at room temperature. The only difference between them is that several typical magnetic parameters at 5 K have been significantly enhanced: the values of M_s, M_r and H_C at 5 K are 2.05 emu g^{-1}, 0.80 emu g^{-1} and 1140 Oe, respectively. We know that the M_s of bulk Ni at 5 K is 58 emu g^{-1}.[58] Based on these magnetic parameters at 5 K and eqn (1), the calculated Ni content is about 3.53%. Obviously, this value is very close to that of 300 K (3.46%). Given the result of Rietveld refinement, *viz.*, 3.66%, the mean value of these three results is 3.55%. Therefore, the synthesized Ni/NiO binary nanoparticles with Ni content of 3.55% and NiO content of 96.45%. The low M_s value is a result of low Ni (or high NiO) content.

It is well known that the particles are single domain and exhibit superparamagnetic feature when the size of ferromagnetic particles is reduced below a critical point.[59] In such situations, once the thermal energy is sufficient to overcome the anisotropy energy barriers, the superparamagnetic phenomenon will happen at a characteristic temperature (called blocking temperature T_B). Previously, the single domain size of nickel particle, 21.2 nm, has been calculated by the magnetic domain theory.[60] Thus, combined with the results of HRTEM observation (particle with size ranging from 5 to 20 nm), the Ni particles in the current Ni/NiO binary nanoparticle system behave like single domain particles. We also measured the ZFC and 500 Oe FC magnetizations of the sample as a function of temperature. As shown in Fig. 4(a), the ZFC/FC curves display irreversible magnetic behavior in the whole temperature range 2–350 K. An increasement of M_{ZFC} but a decreasement of M_{FC} with increasing temperature is observed, and the change in the former is much more obvious than that of the latter. Actually, this behavior is mainly attributed to the thermally activated process of ferromagnetic moments. Firstly, the sample is cooled to 2 K, and thus this process leads to the random distribution of magnetic moments. Then, with increasing temperature, the FM moments try to align in the direction of magnetic field so that the net magnetization gradually increases. Finally, once the cooling process resumed, the FM moments remain locked in the direction of applied field. Therefore, compared with ZFC magnetization (M_{ZFC}), the FC magnetization (M_{FC}) does not change much with the decrease of temperature. It should be noted that the value of T_B depends on the applied magnetic field.[39] Here, no maximum is observed in the ZFC curve, which means that the T_B is above 350 K (namely the upper limit temperature of SQUID testing) in a field of 500 Oe. The above results exhibit the expected behavior of a blocking/freezing process at low temperatures. Similar behaviors are also observed in Fe/Fe-Oxide[61] and other Ni/NiO nanostructures.[39,44,58]

As reported,[35,37–40] the partial magnetic behavior of the Ni/NiO system can be interpreted by considering a disordered NiO component. With regards to the FC curve, the ferromagnetic moments are progressively blocked with decreasing temperature, while the spins of disordered NiO component are frozen in a spin-glass like state. This is consistent with the temperature dependence of M_{FC}. Further, the M_{FC} is almost constant at low temperatures (for example, 2–50 K). The inset in Fig. 4(a) shows the temperature derivative of the difference between the FC and ZFC magnetizations, $-d(M_{FC} - M_{ZFC})/dT$. Such a derivative curve gives a qualitative information on the magnetic behaviors of nanostructures.[61] The peak located at $T_f = 120$ K suggests a frozen disordered magnetic state at low temperatures below this peak. Ahmadvand *et al.* observed T_f values of 45 K and 70 K through the measurements of 10 Oe- and 100 Oe-ZFC/FC curves, respectively, according to Ni/NiO nanoparticles.[39] Here, the T_f value of 120 K corresponds to a magnetic field of 500 Oe. Obviously, the freezing temperature T_f has a strong dependence on the applied magnetic field. Moreover, we also found that in the $-d(M_{FC} - M_{ZFC})/dT$–T curve, where the value keeps going up until 350 K. Here, it points out that the '350 K' is not transition temperature in the true sense. Because the '350 K' is the upper limit temperature of SQUID testing, and thus this curve implies the blocking temperature T_B or the Néel temperature T_N of the present Ni/NiO binary nanoparticles should be higher than 350 K. Analogous phenomena are also observed in various NiO-containing samples.[39,44,45,52] In a word, at low temperatures the

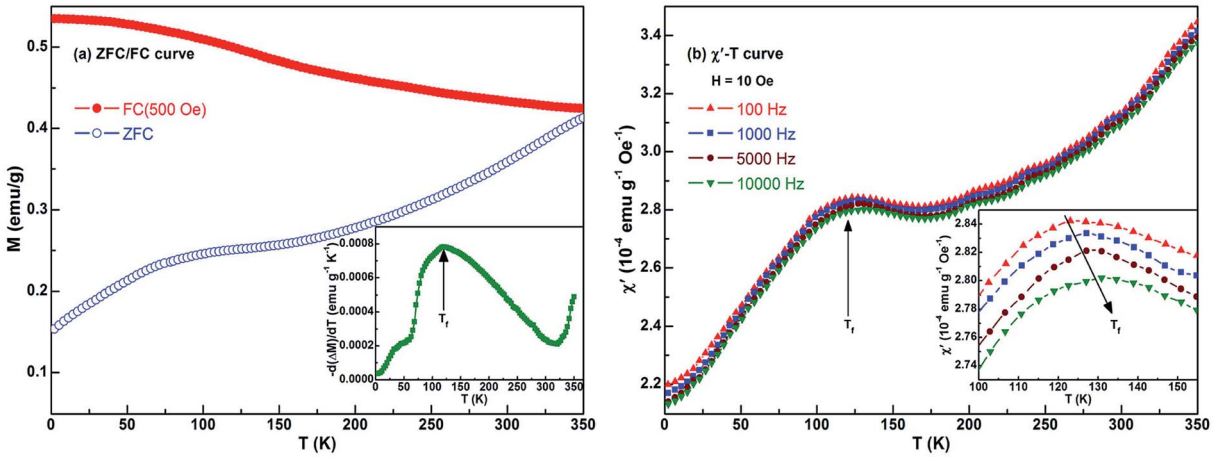

Fig. 4 Temperature dependence of (a) ZFC/FC magnetization and (b) ac susceptibility for Ni/NiO binary nanoparticles. Inset in (a) shows the temperature derivative of the difference between the FC and ZFC magnetizations; inset in (b) depicts that the same curves in the temperature range of 100–155 K after modifying the scales to show the peaks better.

ferromagnetic moments are in the blocked state and a frozen magnetic state is formed in the system.

In order to understand the magnetodynamic properties of the Ni/NiO binary nanoparticles, we studied the temperature and frequency dependence of ac magnetic susceptibility over the obtained sample. Since the time window of the undertaken measurement is determined by the frequency of the ac field, a broad range of time spans can be set by changing the frequency itself.[62] Of particular concern is the real component (χ') of ac susceptibility because it is very sensitive to the change of thermodynamic phase and has often been employed to determine the transition temperature. Fig. 4(b) shows the temperature dependence of χ' at different frequencies. The inset depicts the curves in compressed form covering the 100–155 K intervals to reveal the peak in a better way. For the selected frequencies, all the χ'–T curves give a maximum at $T_f \sim$ 120 K. Strictly speaking, there is a slight increase of T_f with increasing frequency within the adopted temperature range. As shown in the inset in Fig. 4(b), the peaks shift towards a higher temperature with increasing frequency, while the value of χ' decreases. These results are agreement with that of ZFC/FC dc magnetization.

3.3 Influence of temperature on magnetic properties

Fig. 5 shows the ZFC and FC (from 350 K in an applied field of 30 kOe) hysteresis loops, measured at different temperatures, for the Ni/NiO binary nanoparticles. On first sight, the shapes of the complete hysteresis loops in the insets suggest the presence of two components: ferromagnetic Ni and antiferromagnetic NiO. Among them, the linear part responsible for the nonzero slope at high field is ascribable to antiferromagnetic NiO. As can be seen from the enlarged loops, all the ZFC loops are symmetric around the origin whereas all the 30 kOe FC loops are displaced from the origin and broadened. Herein, the value of the displacement defines directly the exchange bias field H_E, and the horizontal broadening can be viewed as the coercivity enhancement ΔH_C ($\equiv H_{C\_FC} - H_{C\_ZFC}$).[9] Large H_E and enhanced H_C are found in the FC case for all test temperatures.

Moreover, the FC loops also undergo vertical shifts relative to the ZFC ones. Similarly, the vertical displacement is regarded as the enhancement in the remanent magnetization, which is $\Delta M_r = M_{r\_FC} - M_{r\_ZFC}$.[34,38] As shown in the enlarged loops in Fig. 5, the evidence of vertical shift for the FC hysteresis loops looks clear. But oddly enough, in Fig. 5 we can only see an increase of the M_r value for the demagnetization branch but not the M_s value. So clearly the present vertical shift is not shift in the true sense, because we cannot see a difference of the M_s between the positive and negative saturation (see the insets in Fig. 5). Indeed, if there is a real vertical shift it means that the external magnetic field applied is not enough to completely orient the system. So, what is the origin of the increase of M_r? One of the most important reasons is that the partial NiO component is considered as a spin-disordered structure with a frozen disordered magnetic state at low temperatures below T_f. So for instance, if we plot, as function of the temperature, the temperature derivative of the remanent magnetization has the same trend as the $-d(M_{FC} - M_{ZFC})/dT$–T curve. Based on the above analysis about ZFC/FC curve, the freezing temperature of 120 K leads to the increase of M_r for the demagnetization branch at low temperatures.

The H_{C_ZFC}, H_{C_FC} and H_E of the sample have strong temperature dependence, as shown in Fig. 6(a). The exchange bias and coercivity do not change much above 100 K. They all gradually decrease with the increase of temperature. The same trend of the temperature dependence of H_C and H_E indicates that the high coercivity may be attributed to the interactions between Ni and NiO components. More specifically, the Ni/NiO binary nanoparticle sample shows a large exchange bias (482 Oe) and enhanced coercivity ($H_{C\_FC} = 1335$ Oe) at 5 K.

Generally speaking, the upper limit of the temperature at which the exchange bias effect may be observed in FM/AFM binary systems is the Néel temperature T_N of AFM bulk.[9] But for the majority of nano-sized AFM materials, the T_N value and

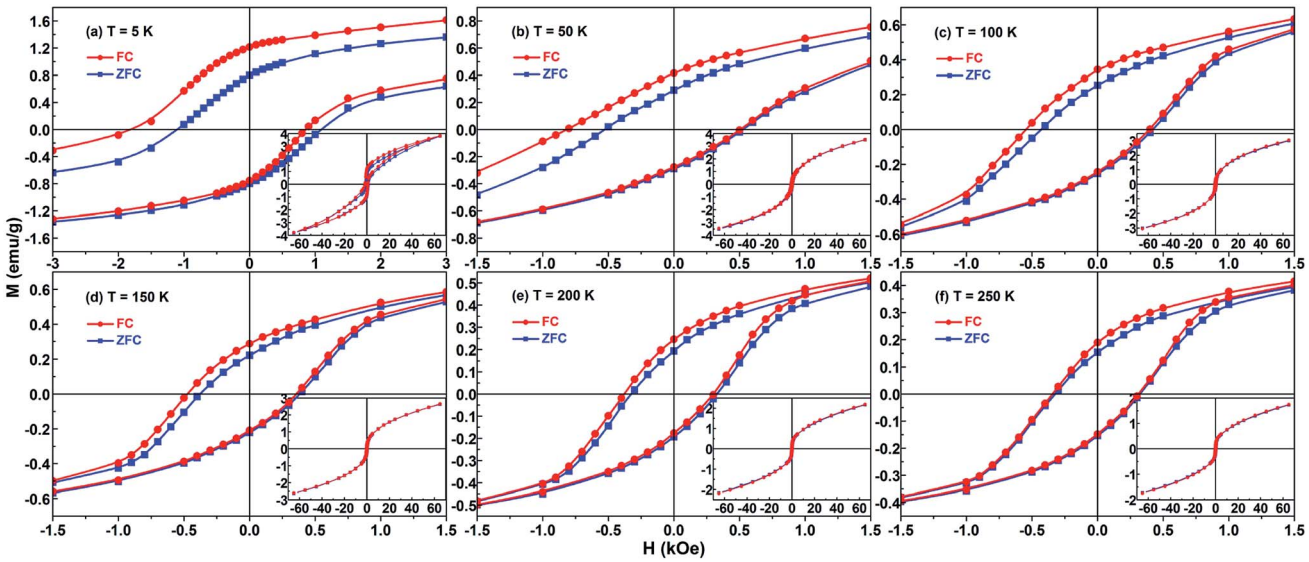

Fig. 5 Hysteresis loops for the Ni/NiO binary nanoparticles measured at different temperatures after ZFC and FC (from 350 K in a cooling field of 30 kOe) processes: the central region of the loops is shown; the complete loops are shown in the insets.

the AFM anisotropy are usually reduced due to the influence of finite-size effect.[63] Therefore the exchange bias phenomenon is often seen to vanish at a temperature far below T_N of the bulk AFM phase. For example, in many conventional Co/CoO systems composed of antiferromagnetic CoO, the exchange bias vanishes at temperatures significantly below T_N ($\approx$293 K) of bulk CoO.[64–66] And for some Ni/NiO systems that have been reported, because the process of sample preparation is difficult to control, a slight and poorly crystallographic AFM NiO component is usually obtained.[36,39] However, the AFM NiO component of current Ni/NiO nanoparticle system is well crystalline and highly contented, giving rise to an excellent FM-AFM interface that is necessary to get the ideal exchange bias at relatively high temperature. Therefore, the exchange bias does not disappear until 250 K in this Ni/NiO particle system, and the specific value of H_E is 16 Oe. Naturally, with this coupling interaction comes certain enhancement of coercivity at different temperatures, as shown in the inset of Fig. 6(a). The value of coercivity enhancement ΔH_C is decreased with increasing temperature, and it reaches the maximum of 237 Oe at 5 K.

Admittedly, exchange bias is an absolutely interface effect, then the microstructure of interface as well as the magnetic states of two phases may be the two most significant factors in regards to changes in EB behavior. Hence, in the present study, most of the magnetic behaviors can be explained through the exchange coupling between ferromagnetic Ni and antiferromagnetic NiO which corresponds to the volume phase. But experiment is full of surprises, there is still some anomalous magnetic behaviors cannot be analyzed according to the usual

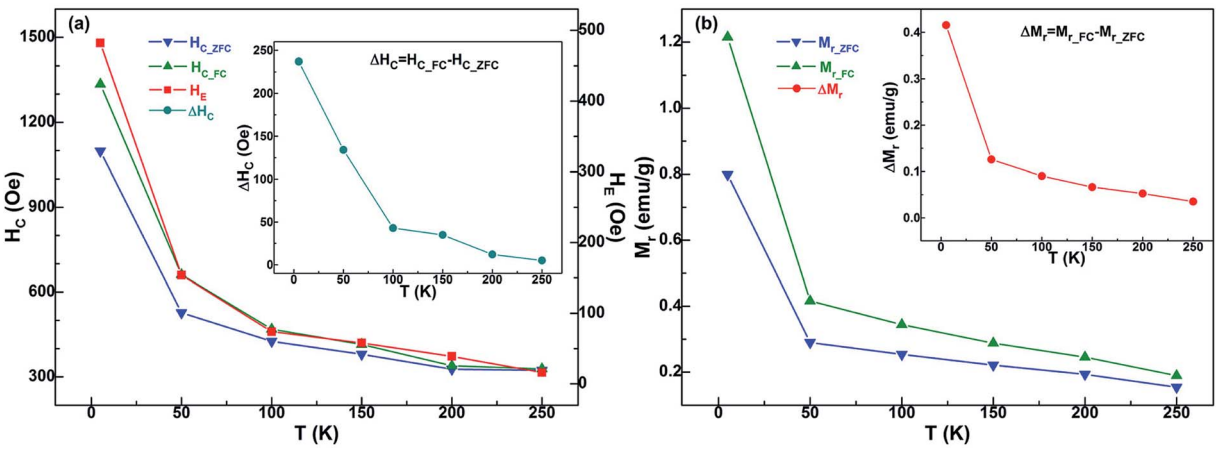

Fig. 6 The temperature dependence of several typical magnetic parameters: (a) the ZFC coercivity H_{C_ZFC}, the FC coercivity H_{C_FC}, the exchange bias H_E, and the coercivity enhancement $\Delta H_C = H_{C\_FC} - H_{C\_ZFC}$; (b) the ZFC remanent magnetization M_{r_ZFC}, the FC remanent magnetization M_{r_FC}, and the difference $\Delta M_r = M_{r\_FC} - M_{r\_ZFC}$.

FM-AFM exchange coupling. For example, the effect of the field cooling on the loops recorded at low temperature is observed only in the first two quadrants but not on the 3rd and 4th, namely, bias disappears once the sample is saturated in a field opposite to that used for the field cooling procedure. Actually, the number of interface spins is very low compared to those occurring in the disordered NiO phase. In other words, this phenomenon is a typical feature of disordered system rather than of exchange bias. Indeed, both hysteresis loops (M–H) and temperature-dependent magnetization curves (M–T) reveal the presence of a very large spin disorder in the structure, which extend well beyond the simple surface of the nanoparticles. This spin disorder can reasonably be the responsible of the shift of the FC loops. This conclusion is consistent with the analysis results of ZFC/FC curves. To sum up, the interesting magnetic behavior for the present Ni/NiO binary nanoparticles is related to the following three factors: (i) the ferromagnetic contribution of Ni nanoparticles, (ii) the intrinsic antiferromagnetism of the volume phase of NiO, and (iii) the spin-glass-like characteristic corresponding to the frozen disordered state at the surface of partial NiO particles.

In general, the shift of a FC loop results in an enhanced positive remanent magnetization (namely the M_{r_FC}) due to pure graphical reasons. As shown in Fig. 5, the FC case determines not only a loop shift, but also an alteration of the loop shape. Herein, the positive remanent magnetization increases, whereas the negative remanent magnetization remain unchanged. Therefore, M_{r_FC} is larger than in the ZFC loop. Similar features have also been observed in other EB-based systems.[34,37,38] In Fig. 6(b), M_{r_FC}, M_{r_ZFC} (the ZFC remanent magnetization) and the difference ΔM_r ($\equiv M_{r\_FC} - M_{r\_ZFC}$) for the Ni/NiO binary nanoparticles is displayed with respect to the test temperature T. These three magnetic parameters revealed the synchronous monotonic decrease with the rise of temperature. Furthermore, the ΔM_r–T curve in the inset of Fig. 6(b) is qualitatively similar to that of H_E (see Fig. 6(a)). This proves the existence of a relation between H_E and ΔM_r, which is a measure of the component of the Ni moment that irreversibly has aligned in the direction of H_{cool} during the FC process, caused by the exchange anisotropy. At 5 K, the ΔM_r value of sample has the highest 0.42 emu g^{-1}. Correspondingly, for the saturation magnetization M_s of the FM Ni component, the calculated value is 2.05 emu g^{-1}, as shown in Fig. 3(b) and the above description. Based on this, the obtained parameter $\Delta M_r/M_s$ is 0.20. Such a relative high ratio is consistent with an excellent combination of the Ni nanoparticles and the NiO nanoparticles, maximizing the FM-AFM Ni/NiO interface. In this case, a larger fraction of the Ni atoms are located at the interface with NiO phase, and the exchange interaction plays a more effective pinning role on the Ni moments. Hence, more Ni moment remains aligned along the cooling field H_{cool}, after removing the applied magnetic field H_{appl} during the low-temperature loop measurement. And then the present Ni/NiO nanoparticle sample at 5 K displays a large exchange bias ($H_E = 482$ Oe), as shown in Fig. 6(a). The above analysis means that the $\Delta M_r/M_s$ ratio also provides some implications on the extent of Ni/NiO interface involved in the EB effect. Analogous agreement between $\Delta M_r/M_s$ and H_E has also been found by Bianco *et al.* in the three Fe/Fe-Oxide nanogranular samples.[61] This demonstrates that the behavior displayed by Ni/NiO nanoparticles is common also to other FM/AFM nanogranular systems formed by using different methods. Based on the distribution of effective anisotropy energy barriers,[58] the spins of NiO component undergo a progressive freezing with the decrease of temperature from 250 K to 5 K. Therefore, the fraction of Ni moments that irreversibly get locked along the direction of cooling field during the FC procedure, which is due to exchange coupling with the frozen NiO spins, increases with decreasing temperature, consistent with the results in Fig. 6. Specifically, for the values of H_E and ΔM_r at low temperatures, both the parameters in Fig. 6 strongly increase for $T < 50$ K, which corresponds to the complete freezing of the spins of the NiO spin-glass-like component.

Considering the pivotal role of exchange bias in such a binary system, the relationship between H_E and temperature has to be studied further theoretically. The results from the effective curve fitting are shown in Fig. 7, which shows a fairly good agreement with the experimental data. The relationship of H_E and T can be expressed as

$$H_E = H_1 \exp(-k_B T/\Delta E_1) + H_2 \exp(-k_B T/\Delta E_2) \quad (2)$$

As shown in Fig. 7, the obtained fitted parameters are $H_1 = 410$ Oe and $H_2 = 160$ Oe, respectively, and k_B denotes the Boltzmann constant (1.38×10^{-23} J K^{-1}). Notice that the contribution of the second exponential term ($e^{-0.0077T}$) is much less than the first ones ($e^{-0.045T}$), especially for the situation of low temperatures (for example, $T \leq 100$ K). So let's do an approximate treatment, eqn (2) can be rewritten as

$$H_E \approx 410 \exp(-k_B T/\Delta E) \quad (3)$$

Substituting the parameters mentioned above into eqn (3), the calculated value of energy barrier ΔE is 1.92 meV. Such an

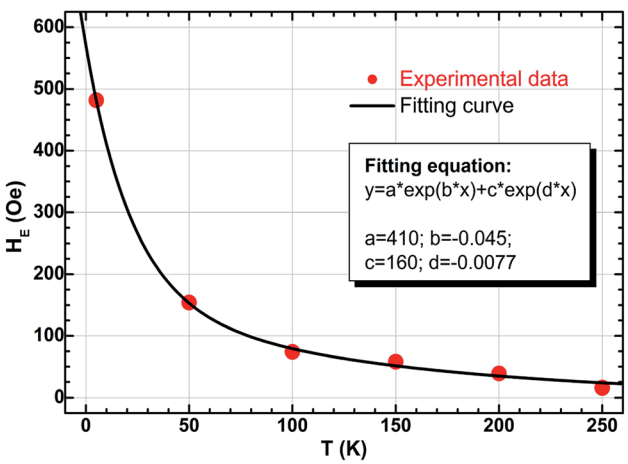

Fig. 7 Temperature dependence of exchange bias H_E together with the fitting curve for the Ni/NiO binary nanoparticles.

energy barrier is very close to the reported values in other systems such as ferromagnet-antiferromagnet bilayers[67,68] and Fe/Fe_3O_4 core–shell magnetic nanoparticles.[69] That means the interface in the present Ni/NiO binary nanoparticles is considerable, and the strongly-coupled FM/AFM interaction is dominant also.

3.4 Influence of cooling field on magnetic properties

As we all know, the change of test temperature T is an important factor that influences the magnetic properties of the EB-based materials, while the other factor is the cooling field H_{cool}. Based on this, FC loops at 5 K for the present Ni/NiO binary nanoparticles were systematically measured after field-cooling process (from 350 K in different H_{cool} values), as shown in Fig. 8. On the whole, all the FC loops exhibit the same loop shape and magnetic feature, whereas the only differences are the magnitudes of the specific magnetic parameters such as coercivity and exchange bias. In order to obtain further information about these two parameters, the insets in Fig. 8 depict the enlarged view of the central region of loops.

In Fig. 9 the values of FC coercivity H_{C_FC} and exchange bias H_E at 5 K are plotted as a function of cooling field H_{cool}, where these two parameters show a synchronous change trend. More specifically, H_E firstly increases sharply and then decreases slowly with increasing cooling field, and it maximally taking value ($H_E(max) = 482$ Oe) at $H_{cool} = 30$ kOe. Correspondingly, H_{C_FC} increases initially and then decreases up to 10% for the increase of H_{cool} from 30 to 60 kOe, and the maximum value is $H_{C\_FC}(max) = 1335$ Oe. Needs to be emphasized that the above two quantities are relatively large for the Ni/NiO systems, compared to many previous reports.[31,43–45,51]

Herein the EB behaviors exhibited by the present Ni/NiO binary nanoparticles are similar to the cooling field dependence of exchange bias effect in other Ni/NiO nanostructure and Fe/Fe-Oxides core–shell structure.[37,70] Where the EB effect reported by Bianco *et al.* is involved with ferromagnetic core and spin-glass or disordered magnetic shell. The shift of hysteresis loop is due to the pinning of the FM spins at the interface by the intrinsic AFM or SG spins when the sample is cooled down to low temperature during the FC procedure. In the case of small H_{cool} (such as <30 kOe here), H_E increases sharply with increasing H_{cool}, which is ascribed to the alignment of pinned FM spins toward the direction of cooling field. When all the pinned spins are aligned, the increase of cooling field cannot conduce to the increase of H_E above a certain limit of H_{cool}. While for the large H_{cool} (such as ≥30 kOe here), it strongly influences the spins of spin-glass or disordered magnetic components, leading to an appreciable decrease of H_E. These phenomena have also been observed in various EB-based systems involved with the FM/SG (or FM/disordered magnetic structure) interface.[70–72]

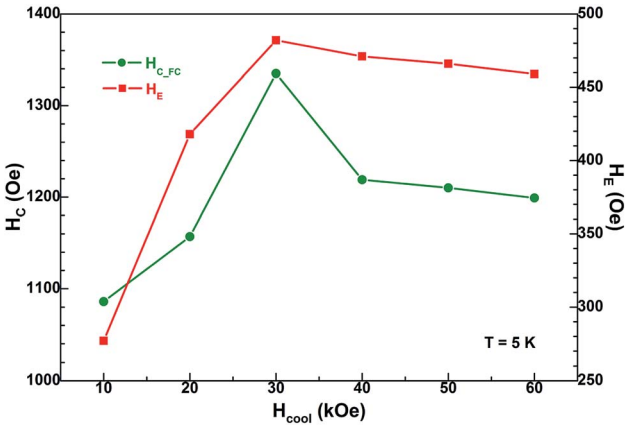

Fig. 9 Cooling field dependence of FC coercivity H_{C_FC} and exchange bias H_E.

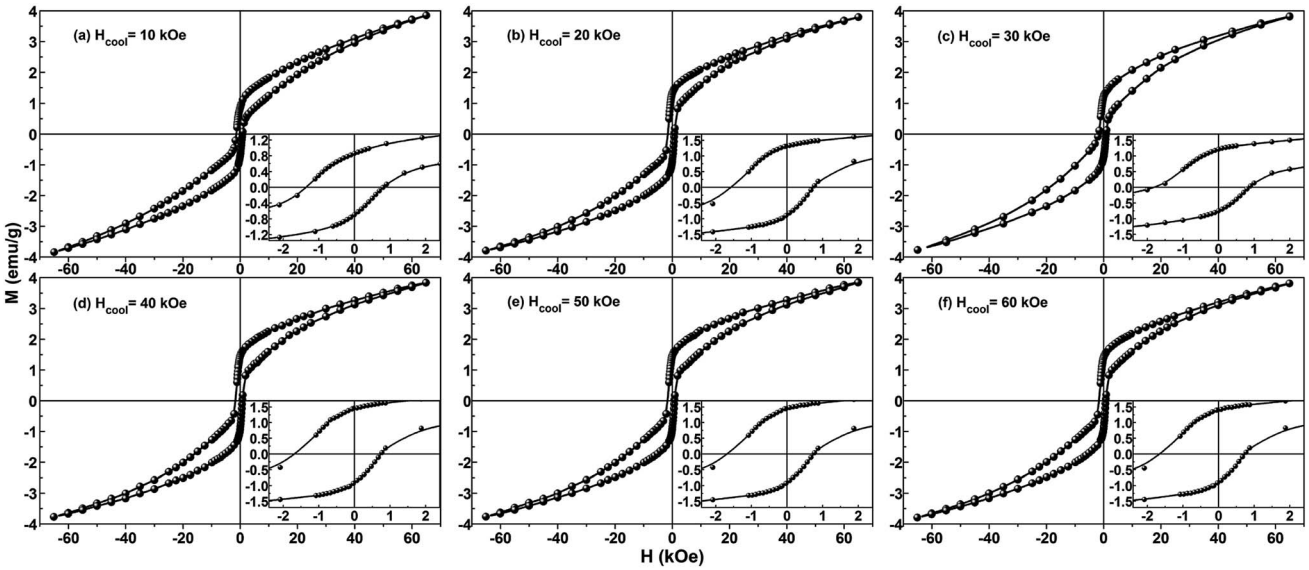

Fig. 8 Hysteresis loops for the Ni/NiO binary nanoparticles measured at 5 K after FC process (from 350 K in different cooling fields H_{cool}); insets are the enlarged view of the central region of loops.

If one assumes that the phenomenology of exchange bias is an absolutely interface effect, then the microstructure of interface as well as the magnetic states of two phases may be the two most significant factors in regards to changes in EB behavior. On one hand, the appearance of exchange bias effect depends on the modes of microstructure; for instance, direct physical contact or the nanoparticles embedded in a matrix.[11] For the Co/CoO core–shell nanostructures embedded in the matrices, however, the magnetic properties reported by many works also have huge differences.[11,73–75] The Ni/NiO nanostructure prepared by using ball-milling method shows a large H_E because of the Ni and NiO nanograins are in direct physical contact.[58,76] In the present work, the TEM investigation of the Ni/NiO binary nanoparticles indicates that the sample has an excellent Ni/NiO interface, as well as the Ni and NiO nanocrystallines have better contact with each other, which may lead to the observed large value of H_E accompanied with an enhanced value of H_C. On the other hand, the EB-based structures must have two different magnetic phases, which corresponds to the reversible spins with low magnetic anisotropy and the rigid spins having strong anisotropy. Considering the current Ni/NiO nanoparticle sample that contains the ferromagnetic Ni component whose spins are reversible whereas the NiO components have moderately stronger anisotropic spins due to the nanoscale size of the NiO particles.[58,76,77] Compared with CoO, such a weaker anisotropy of NiO has important role on the EB effect. To sum up, with change of temperature and cooling field, several important magnetic parameters such as M_r, H_C and H_E demonstrate complicated characteristics, which is mainly due to the interface interaction of Ni and NiO phases. Therefore for the current Ni/NiO binary nanoparticles, three magnetic structures – ferromagnetic Ni nanoparticles, antiferromagnetic NiO nanoparticles, and the glassy magnetic disordered NiO particles – compete with each other and promote the generation of exchange bias and the enhancement of coercivity.

4. Conclusions

Ni/NiO binary nanoparticles were synthesized by a reflux process using nickel acetate tetrahydrate and ethylene glycol as the precursor and the solvent, respectively. Their microstructures and magnetic properties were systematically investigated by XRD, XPS, SEM, HRTEM, VSM, SQUID and PPMS. The size of Ni and NiO crystallites is 5–20 nm and the relative Ni content is about 3.55%, and the sample has excellent Ni/NiO interface. At 5 K, the Ni/NiO binary nanoparticles show a large exchange bias (482 Oe) and enhanced coercivity (1335 Oe). According to the analysis on the ZFC/FC curves, χ'–T curves and M–H loops, the change rules of all the parameters such as T_f, H_{C_ZFC}, H_{C_FC}, ΔH_C, H_E, M_{r_ZFC}, M_{r_FC}, ΔM_r and $\Delta M_r/M_s$ indicate a complicated magnetic behavior. The changes of the FC coercivity H_{C_FC} and the exchange bias H_E show a synchronous trend with varying temperature and cooling field, which is due to the coupling interaction at the Ni/NiO interface. The Ni/NiO binary nanoparticle studied in this report is a strongly coupled system, where the interaction is related to the following three factors: (i) the ferromagnetic component corresponding to all the Ni nanoparticles; (ii) the antiferromagnetic behavior corresponding to the NiO volume phase; and (iii) the glassy magnetic character exhibited by the frozen disordered state at the surface of NiO particles. Finally, at low temperatures the ferromagnetic Ni moments are in the blocked state along the direction of cooling field during the FC procedure, while the spins of disordered NiO component are frozen in a spin-glass like state.

Conflicts of interest

There are no conflicts to declare.

Acknowledgements

We would like to thank the High Magnetic Field Laboratory, Chinese Academy of Sciences for SQUID measurement. This work was financially supported by the National Natural Science Foundation (Grant Nos. 11604160 and 11474151), the Natural Science Foundation of Jiangsu Province (Grant No. BK20160876), the Scientific Research Foundation of Nanjing University of Posts and Telecommunications (NUPTSF, Grant No. NY215063), and the Open Project for National Laboratory of Solid State Microstructures, Nanjing University (Grant No. M30007), P. R. China.

References

1 Y. H. Ting, J. Y. Chen, C. W. Huang, T. K. Huang, C. Y. Hsieh and W. W. Wu, *Small*, 2018, **14**, 1703153.
2 Y. X. Zeng, Y. Meng, Z. Z. Lai, X. Y. Zhang, M. H. Yu, P. P. Fang, M. M. Wu, Y. X. Tong and X. H. Lu, *Adv. Mater.*, 2017, **29**, 1702698.
3 Y. Rho, K. T. Kang and D. Lee, *Nanoscale*, 2016, **8**, 8976–8985.
4 Y. Liu, N. Q. Fu, G. G. Zhang, W. Lu, L. M. Zhou and H. T. Huang, *J. Mater. Chem. A*, 2016, **4**, 15049–15056.
5 Y. J. Zhang, J. H. Chen, L. L. Li, J. Ma, C. W. Nan and Y. H. Lin, *Phys. Rev. B*, 2017, **95**, 174420.
6 K. Nadeem, A. Ullah, M. Mushtaq, M. Kamran, S. S. Hussain and M. Mumtaz, *J. Magn. Magn. Mater.*, 2016, **417**, 6–10.
7 J. P. Domann, W. Y. Sun, L. T. Schelhas and G. P. Carman, *J. Appl. Phys.*, 2016, **120**, 143904.
8 A. C. Gandhi and J. G. Lin, *J. Phys.: Condens. Matter*, 2017, **29**, 215802.
9 J. Nogués, J. Sort, V. Langlais, V. Skumryev, S. Suriñach, J. S. Muñoz and M. D. Baró, *Phys. Rep.*, 2005, **422**, 65–117.
10 M. C. Spadaro, S. D'Addato, P. Luches, S. Valeri, V. Grillo, E. Rotunno, M. A. Roldan, S. J. Pennycook, A. M. Ferretti, E. Capetti and A. Ponti, *Nanotechnology*, 2015, **26**, 405704.
11 V. Skumryev, S. Stoyanov, Y. Zhang, G. Hadjipanayis, D. Givord and J. Nogués, *Nature*, 2003, **423**, 850–853.
12 A. Roy, J. A. De Toro, V. S. Amaral, P. Muniz, J. M. Riveiro and J. M. F. Ferreira, *J. Appl. Phys.*, 2014, **115**, 073904.
13 W. H. Meiklejohn and C. P. Bean, *Phys. Rev.*, 1956, **102**, 1413–1414.
14 S. Peng, C. Wang, J. Xie and S. H. Sun, *J. Am. Chem. Soc.*, 2006, **128**, 10676–10677.
15 B. D. Cullity and C. D. Graham, *Introduction to Magnetic Materials*, IEEE Press, New Jersey, 2009.

16 M. S. Lund, W. A. A. Macedo, K. Liu, J. Nogués, I. K. Schuller and C. Leighton, *Phys. Rev. B*, 2002, **66**, 054422.
17 Q. Li, C. L. Liang, X. F. Lu, Y. X. Tong and G. R. Li, *J. Mater. Chem. A*, 2015, **3**, 6432–6439.
18 C. Rinsha, C. N. Anumol, M. Chithra, B. N. Sahu and S. C. Sahoo, *AIP Conf. Proc.*, 2015, **1665**, 050119.
19 F. G. Liu, X. B. Wang, J. Hao, S. Han, J. S. Lian and Q. Jiang, *Sci. Rep.*, 2017, **7**, 17709.
20 H. T. Das, K. Mahendraprabhu, T. Maiyalagan and P. Elumalai, *Sci. Rep.*, 2017, **7**, 15342.
21 F. Ghaemi, L. C. Abdullah and P. Tahir, *Polymers*, 2016, **8**, 381.
22 M. K. Singh, A. Agarwal, R. K. Swarnkar, R. Gopal and R. K. Kotnala, *Sci. Adv. Mater.*, 2012, **4**, 532–536.
23 Y. Z. Zhou, J. S. Chen, B. K. Tay, J. F. Hu, G. M. Chow, T. Liu and P. Yang, *Appl. Phys. Lett.*, 2007, **90**, 043111.
24 C. L. Yuan, *J. Phys. Chem. C*, 2010, **114**, 2124–2126.
25 R. M. Silva, R. A. Raimundo, W. V. Fernandes, S. M. Torres, V. D. Silva, J. P. F. Grilo, M. A. Morales and D. A. Macedo, *Ceram. Int.*, 2018, **44**, 6152–6156.
26 K. Mahendraprabhu and P. Elumalai, *J. Sol-Gel Sci. Technol.*, 2015, **73**, 428–433.
27 J. Yu, Y. H. Ni and M. H. Zhai, *J. Phys. Chem. Solids*, 2018, **112**, 119–126.
28 V. G. Prabhu, P. S. Shajira, N. Lakshmi and M. J. Bushiri, *J. Phys. Chem. Solids*, 2015, **87**, 238–243.
29 A. Roy, J. A. De Toro, V. S. Amaral, D. P. Marques and J. M. F. Ferreira, *J. Appl. Phys.*, 2014, **116**, 093906.
30 F. F. Yuan, Y. H. Ni, L. Zhang, S. M. Yuan and J. D. Wei, *J. Mater. Chem. A*, 2013, **1**, 8438–8444.
31 B. M. Abu-Zied and A. M. Asiri, *Thermochim. Acta*, 2017, **649**, 54–62.
32 A. D. Khalaji, G. Grivani and S. Izadi, *J. Therm. Anal. Calorim.*, 2016, **126**, 1105–1109.
33 A. E. Berkowitz and K. Takano, *J. Magn. Magn. Mater.*, 1999, **200**, 552–570.
34 L. Del Bianco, F. Spizzo, M. Tamisari and S. Laureti, *Solid State Commun.*, 2011, **151**, 351–353.
35 A. C. Johnston-Peck, J. W. Wang and J. B. Tracy, *ACS Nano*, 2009, **3**, 1077–1084.
36 H. C. Hsu, C. C. Lo and Y. C. Tseng, *J. Appl. Phys.*, 2012, **111**, 063919.
37 M. Thakur, M. Patra, S. Majumdar and S. Giri, *J. Alloys Compd.*, 2009, **480**, 193–197.
38 L. Del Bianco, F. Spizzo, M. Tamisari and A. Castiglioni, *J. Appl. Phys.*, 2011, **110**, 043922.
39 H. Ahmadvand, H. Salamati, P. Kameli and F. S. Razavi, *J. Supercond. Novel Magn.*, 2010, **23**, 1467–1471.
40 A. Querejeta-Fernández, M. Parras, A. Varela, F. del Monte, M. García-Hernández and J. M. González-Calbet, *Chem. Mater.*, 2010, **22**, 6529–6541.
41 Joint Committee on Powder Diffraction Standards (JCPDS) card no. 04-0850.
42 Joint Committee on Powder Diffraction Standards (JCPDS) card no. 47-1049.
43 X. Xiang, X. T. Zu, S. Zhu and L. M. Wang, *Phys. B*, 2005, **368**, 88–93.
44 V. Ganeshchandra Prabhu, A. Rasheed Paloly, N. G. Divya and M. Junaid Bushiri, *Mater. Sci. Eng., B*, 2018, **228**, 132–141.
45 M. Patange, S. Biswas, A. K. Yadav, S. N. Jha and D. Bhattacharyya, *Phys. Chem. Chem. Phys.*, 2015, **17**, 32398–32412.
46 A. Kremenović, B. Jančar, M. Ristić, M. Vučinić-Vasić, J. Rogan, A. Pačevski and B. Antić, *J. Phys. Chem. C*, 2012, **116**, 4356–4364.
47 V. Perebeinos, S. W. Chan and F. Zhang, *Solid State Commun.*, 2002, **123**, 295–297.
48 M. A. Peck and M. A. Langell, *Chem. Mater.*, 2012, **24**, 4483–4490.
49 S. Biswas, V. Srivastava and S. Ram, *J. Phys. Chem. C*, 2007, **111**, 7593–7598.
50 H. S. Nalwa, *Handbook of Nanostructured Materials and Nanotechnology*, Academic Press, San Diego, CA, 1994, p. 179.
51 M. R. Salvadori, R. A. Ando, D. Muraca, M. Knobel, C. A. O. Nascimento and B. Corrêa, *RSC Adv.*, 2016, **6**, 60683–60692.
52 X. J. Yao, X. M. He, X. Y. Song, Q. Ding, Z. W. Li, W. Zhong, C. T. Au and Y. W. Du, *Phys. Chem. Chem. Phys.*, 2014, **16**, 6925–6930.
53 D. Olszewska, *Fuel Process. Technol.*, 2012, **95**, 90–95.
54 M. Lenglet, F. Hochu, J. Dürr and M. H. Tuilier, *Solid State Commun.*, 1997, **104**, 793–798.
55 O. Kuschel, R. Buß, W. Spiess, T. Schemme, J. Wöllermann, K. Balinski, A. T. N'Diaye, T. Kuschel, J. Wollschläger and K. Kuepper, *Phys. Rev. B*, 2016, **94**, 094423.
56 S. A. Makhlouf, H. Al-Attar and R. H. Kodama, *Solid State Commun.*, 2008, **145**, 1–4.
57 A. Roy, V. Srinivas, S. Ram and T. V. C. Rao, *J. Phys.: Condens. Matter*, 2007, **19**, 346220.
58 L. Del Bianco, F. Boscherini, A. L. Fiorini, M. Tamisari, F. Spizzo, M. V. Antisari and E. Piscopiello, *Phys. Rev. B*, 2008, **77**, 094408.
59 A. H. Morrish, *The Physical Principles of Magnetism*, IEEE, New York, 2001.
60 K. V. P. M. Shafi, A. Gedanken, R. Prozorov and J. Balogh, *Chem. Mater.*, 1998, **10**, 3445–3450.
61 L. Del Bianco, D. Fiorani, A. M. Testa, E. Bonetti, L. Savini and S. Signoretti, *Phys. Rev. B*, 2002, **66**, 174418.
62 S. Thota and J. Kumar, *J. Phys. Chem. Solids*, 2007, **68**, 1951–1964.
63 J. Nogués and I. K. Schuller, *J. Magn. Magn. Mater.*, 1999, **192**, 203–232.
64 M. Feygenson, Y. Yiu, A. Kou, K. S. Kim and M. C. Aronson, *Phys. Rev. B*, 2010, **81**, 195445.
65 M. Kovylina, M. G. del Muro, Z. Konstantinović, M. Varela, Ò. Iglesias, A. Labarta and X. Batlle, *Nanotechnology*, 2009, **20**, 175702.
66 S. Chandra, H. Khurshid, M. H. Phan and H. Srikanth, *Appl. Phys. Lett.*, 2012, **101**, 232405.
67 M. D. Stiles and R. D. McMichael, *Phys. Rev. B*, 1999, **60**, 12950.

68 J. Dubowik, F. Stobiecki, I. Gościańska, Y. P. Lee, A. Paetzold and K. Röll, *Eur. Phys. J. B*, 2005, **45**, 283.
69 Q. K. Ong, A. Wei and X. M. Lin, *Phys. Rev. B*, 2009, **80**, 134418.
70 L. Del Bianco, D. Fiorani, A. M. Testa, E. Bonetti and L. Signorini, *Phys. Rev. B*, 2004, **70**, 052401.
71 M. Patra, K. De, S. Majumdar and S. Giri, *Eur. Phys. J. B*, 2007, **58**, 367–371.
72 M. Thakur, M. Patra, K. De, S. Majumdar and S. Giri, *J. Phys.: Condens. Matter*, 2008, **20**, 195215.
73 J. Nogués, V. Skumryev, J. Sort, S. Stoyanov and D. Givord, *Phys. Rev. Lett.*, 2006, **97**, 157203.
74 J. B. Tracy, D. N. Weiss, D. P. Dinega and M. G. Bawendi, *Phys. Rev. B*, 2005, **72**, 064404.
75 A. N. Dobrynin, D. N. Ievlev, K. Temst, P. Lievens, J. Margueritat, J. Gonzalo, C. N. Afonso, S. Q. Zhou, A. Vantomme, E. Piscopiello and G. Van Tendeloo, *Appl. Phys. Lett.*, 2005, **87**, 012501.
76 L. Del Bianco, F. Boscherini, M. Tamisari, F. Spizzo, M. Vittori Antisari and E. Piscopiello, *J. Phys. D: Appl. Phys.*, 2008, **41**, 134008.
77 R. H. Kodama, S. A. Makhlouf and A. E. Berkowitz, *Phys. Rev. Lett.*, 1997, **79**, 1393–1396.